Research Square

Preprints are preliminary reports that have not undergone peer review.
They should not be considered conclusive, used to inform clinical practice,
or referenced by the media as validated information.

Multivariate Optimization of the Synthesis of ZnCl 2 -Activated Biochar Functionalized with Bimetallic Au-Ag Nanoparticles for Catalytic Application in the Reduction of p-Nitrophenol

Daliane Cláudia Faria
Universidade Federal de Viçosa (UFV)
Antonio Machado Netto
Universidade Federal de Viçosa (UFV)
Igor Pecly Estephaneli
Universidade Federal de Viçosa (UFV)
Ana Luíza Quintão Santos
Universidade Federal de Viçosa (UFV)
Fernanda Bicalho Almeida Papa
Universidade Federal de Viçosa (UFV)
Frederico Garcia Pinto
Institute of Exact and Technological Sciences, Universidade Federal de Viçosa (UFV)
Renata Pereira Lopes Moreira
renata.plopes@ufv.br

Universidade Federal de Viçosa (UFV)

Research Article

Keywords: Agro-industrial residues, Waste valorization, Sustainable materials, Heterogeneous catalysis, Environmental remediation, Nanomaterials, Circular economy

Posted Date: November 19th, 2026

DOI: https://doi.org/10.21203/rs.3.rs-11168451/v1

License: This work is licensed under a Creative Commons Attribution 4.0 International License.
Read Full License

Additional Declarations: No competing interests reported.

Multivariate Optimization of the Synthesis of $ZnCl_2$-Activated Biochar Functionalized with Bimetallic Au-Ag Nanoparticles for Catalytic Application in the Reduction of *p*-Nitrophenol

Daliane Cláudia de Faria[a], Antonio Machado Netto[a], Igor Pecly Estephaneli[a], Ana Luíza Quintão Santos[a], Fernanda Bicalho Almeida Papa[a], Frederico Garcia Pinto [b], Renata Pereira Lopes Moreira[a]*

[a]*Department of Chemistry, Universidade Federal de Viçosa (UFV), Av. Peter Henry Rolfs, s/n, Campus Universitário, 36570-900 Viçosa-MG, Brazil.*

[b]*Institute of Exact and Technological Sciences, Universidade Federal de Viçosa (UFV), Rodovia MG230 - Km 8, Campus Rio Paranaíba, 38810-000 Rio Paranaíba-MG, Brazil.*

Corresponding author:
Renata Pereira Lopes Moreira
E-mail: renata.plopes@ufv.br

GRAPHICAL ABSTRACT



ABSTRACT

The valorization of agro-industrial residues to produce carbonaceous materials offers a sustainable route for developing heterogeneous catalysts. In this study, passion fruit peel was used as a precursor for $ZnCl_2$-activated biochar, whose synthesis was optimized using a Central Composite Rotatable Design (CCRD), considering carbonization temperature, residence time, and impregnation ratio. The optimized conditions were 525 °C, 60 min, and a biomass-to-$ZnCl_2$ impregnation ratio of 2.0 (w/w). The resulting optimized biochar (BC-OT) exhibited a high specific surface area of 1411.64 $m^2\ g^{-1}$. Pyrolysis promoted carbon enrichment, reduced the H/C and O/C ratios to 0.338 and 0.381. BC-OT showed a point of zero charge (pH_{PZC}) of 6.53 and a lactonic group content of 1.50 mmol g^{-1}. The biochar was subsequently functionalized with Au and Ag nanoparticles (NPs) and applied as a heterogeneous catalyst for the $NaBH_4$-mediated reduction of *p*-nitrophenol. For $Au_{0.5}$-$Ag_{0.5}$ NPs/BC-OT, EDS confirmed the presence of Au and Ag, while HRTEM revealed nanoparticles with an average diameter of 7.4 ± 3.4 nm. Lattice fringes and SAED patterns showed interplanar spacings consistent with face-centered cubic Au and/or Ag domains and wurtzite ZnO. Among the evaluated materials, 50:50 Ag:Au exhibited the highest apparent rate constant (k_{app}) of (15.18 ± 2.27) × 10^{-3} s^{-1}, outperforming the monometallic catalysts and the non-functionalized support. The catalyst remained active over four reuse cycles. These results demonstrate the potential of passion fruit peel as a renewable precursor for porous carbonaceous supports containing Au-Ag nanoparticles for the catalytic reduction of nitroaromatic compounds.

Keywords: Agro-industrial residues; Waste valorization; Sustainable materials; Heterogeneous catalysis; Environmental remediation; Nanomaterials; Circular economy.

1. INTRODUÇÃO

The global population reached 7.9 billion in 2022 and is projected to reach 8.6 billion by 2032 (OECD-FAO, 2023). This growth has increased food demand and driven agricultural production, which rose by 61% between 1990 and 2019, exceeding the 45% population increase over the same period (Sands et al., 2023). Consequently, agro-industrial waste generation is also increasing, reinforcing the need for valorization strategies aligned with sustainability and the circular economy. Such strategies can convert residual biomass into higher-value products while reducing the environmental impacts associated with improper waste disposal (Sharma et al., 2025; Zhang et al., 2024). This approach also contributes to Sustainable Development Goals (SDGs) 6, 12, 13, and 15 (UNITED NATIONS, 2015).

Among Brazilian fruit chains, yellow passion fruit (*Passiflora edulis*) is particularly relevant (Lobo et al., 2025). In 2024, Brazil produced approximately 736.5 thousand tonnes, with a production value of approximately US$416 million (de Almeida et al., 2026). However, approximately 65–70% of the fresh fruit mass may become waste during processing, mainly peel and seeds (Cabral et al., 2025). The peel contains cellulose, hemicellulose, pectin, and phenolic compounds, making it a suitable precursor for carbonaceous materials with greater technological value (Fan et al., 2025).

An alternative approach for valorizing this biomass is its conversion into biochar, a carbon-rich solid material produced by the thermochemical conversion of biomass under oxygen-limited conditions (Morim et al., 2025). Its properties depend on the feedstock and synthesis conditions, including specific surface area, porosity, chemical stability, and surface functional groups (Zhu et al., 2024). These properties are important for environmental (Sun et al., 2025), energy-related (Aslam et al., 2025), and catalytic applications (Zhu et al., 2024).

Biochars can be produced by torrefaction, hydrothermal carbonization, gasification, and pyrolysis, the latter being one of the most widely used routes (Escalante et al., 2026). Pyrolysis involves the thermal decomposition of biomass, typically at 300–700 °C under limited oxygen availability, promoting carbon enrichment of the resulting solid fraction (Morim et al., 2025). The operating temperature, heating rate, and residence time strongly influence key properties, including surface composition and pore structure (Cabral et al., 2025). Beyond these pyrolysis parameters, chemical activation with $ZnCl_2$ can enhance pore development because this agent acts as a dehydrating agent, favoring the removal of volatile components and the formation and enlargement of pores in the carbon matrix (Samghouli et al., 2025; Wu et al., 2023).

These properties make biochars promising materials for a wide range of water treatment applications (Zhou et al., 2024), contaminant adsorption (Chandravanshi et al., 2026), soil remediation (Skjennum et al., 2026), carbon capture (Cheng et al., 2026), energy storage (Atinafu et al., 2025) and catalysis (Osire & Gnaro, 2026). For passion fruit peel, materials have already been reported for CO_2 capture (Peres et al., 2024) and dye adsorption (Cabral et al., 2025). In addition, biochars can be used as support for heterogeneous catalysts, promoting the dispersion and immobilization of metal nanoparticles (Lavorato et al., 2026).

Ag and Au nanoparticles, including bimetallic systems, have shown promising catalytic activity toward the reduction of nitroaromatic compounds (Lyu et al., 2023). Among the model reactions used to evaluate these systems, the reduction of p-nitrophenol (p-NP) to p-aminophenol (p-AP) by $NaBH_4$ is particularly relevant (Strachan et al., 2020). The widespread use of p-NP in the production of pesticides, dyes, and pharmaceuticals has raised environmental concerns, as this compound is considered a priority pollutant due to its toxicity and persistence in the environment (Badamasi et al., 2025). In the

absence of a catalyst, the reduction proceeds slowly, making it a suitable model reaction for UV–Vis spectrophotometric monitoring and the evaluation of catalytic performance through apparent rate constants (Strachan et al., 2020).

In this context, this work presents an integrated approach involving the multivariate optimization of activated biochar derived from passion fruit peel, its functionalization with Ag–Au nanoparticles, and the evaluation of its catalytic performance in p-NP reduction. The novelty lies in integrating agro-industrial waste valorization, the simultaneous optimization of biochar production conditions using a Central Composite Rotatable Design, and the development of a bimetallic Ag–Au catalytic system supported on a porous carbon matrix. The underlying hypothesis is that $ZnCl_2$ activation combined with pyrolysis promotes the formation of a porous matrix suitable for nanoparticle immobilization, while the combination of Ag and Au provides efficient catalytic sites for p-NP reduction. Therefore, the objective of this work was to optimize the production of $ZnCl_2$-activated passion fruit peel biochar using a Central Composite Rotatable Design, functionalize the optimized biochar with Au–Ag nanoparticles, and evaluate its performance in the catalytic reduction of p-NP by $NaBH_4$.

2. MATERIALS AND METHODS

2.1. Chemicals and reagents

All reagents were analytical grade. Anhydrous zinc chloride ($ZnCl_2$; 96%; CAS 7646-85-7) was purchased from Êxodo Científica, Sumaré, São Paulo, Brazil. p-Nitrophenol ($C_6H_5NO_3$; 98.00%; CAS 100-02-7) was obtained from Êxodo Científica, Hortolândia, São Paulo, Brazil. Sodium hydroxide (NaOH; 99.00%; CAS 1310-73-2) was purchased from ACS Científica, Sumaré, São Paulo, Brazil. Sodium borohydride ($NaBH_4$; 98.00%; CAS 16940-66-2) and silver nitrate ($AgNO_3$; 99.00%; CAS 7761-88-

8) were purchased from Neon, Suzano, São Paulo, Brazil. Potassium chloride (KCl; 99.00%; CAS 7447-40-7) was purchased from Merck, São Paulo, Brazil. Hydrogen tetrachloroaurate(III) trihydrate ($HAuCl_4 \cdot 3H_2O$; 99.90%; CAS 16961-25-4) was purchased from Sigma-Aldrich, Cotia, São Paulo, Brazil. Hydrochloric acid (HCl; 35%; CAS 7647-01-0) was purchased from Dinâmica, Indaiatuba, São Paulo, Brazil.

All solutions were prepared using ultrapure water obtained from a Milli-Q system (Millipore, Bedford, MA, USA).

2.2. Biochar production

Passion fruit peels were obtained from a juice and pulp processing facility in the region (Tial – Visconde do Rio Branco, Minas Gerais, Brazil) and dried at 100 °C for 16 h. The material was subsequently ground and sieved through a 10-mesh sieve.

The experimental variables used in the CCRD, with three center points (n = 3), to optimize biochar synthesis were: (1) carbonization temperature (450 – 550 °C), (2) residence time (45 – 75 min), and (3) $ZnCl_2$ impregnation ratio, defined as the mass ratio of activating agent to biomass, ranging from 1 to 3, as shown in Table 1. The heating rate was kept constant at 5 °C min^{-1}.

The predetermined amounts of $ZnCl_2$ and biomass were weighed and thoroughly homogenized with enough water to ensure complete mixing. The samples were then dried in an oven at 100 °C for 24 h. Subsequently, the samples were placed in covered crucibles and pyrolyzed in a muffle furnace under the conditions described in Table 1. Thermal treatment was performed in a muffle furnace (Lucadema, São José do Rio Preto, São Paulo, Brazil). For particle-size standardization, a 500 μm sieve (35 ABNT or 32 mesh; Bertel, Caieiras, São Paulo, Brazil) was used.

The resulting material was subsequently treated with 300 mL of HCl solution (0.100 mol L^{-1}) and maintained under magnetic stirring for 1 h. The material was subsequently washed with water until the filtrate pH reached 6.5 – 7.5. The samples were then dried in an oven at 105 °C for 24 h, ground using a mortar and pestle, and sieved again through a 32-mesh sieve.

Table 1. Biochar production conditions based on the Central Composite Rotatable Design

Sample	Temperature (°C)	Time (min)	Impregnation ratio
1	500	75	2.00
2	470	69	2.59
3	500	60	1.00
4	530	51	2.59
5	530	51	1.40
6	500	45	2.00
7	550	60	2.00
8	470	51	2.59
9	530	69	2.59
10	500	60	2.00
11	450	60	2.00
12	500	60	3.00
13	470	51	1.40
14	470	69	1.40
15	500	60	2.00
16	530	69	1.40
17	500	60	2.00

The samples were weighed before pyrolysis (Eq. 1) and after the post-pyrolysis washing step (Eq. 2) to calculate process yield.

$$\textbf{Pyrolysis yield}\ (\%) = \frac{(m_{biomass+ZnCl_2})_{After\ pyrolysis}}{(m_{biomass+ZnCl_2})_{Before\ pyrolysis}} \times 100 \qquad \text{(Eq. 1)}$$

$$\textbf{Final yield}\ (\%) = \frac{(m_{biochar})_{After\ washing\ step}}{(m_{biomass})_{Before\ pyrolysis}} \times 100 \qquad \text{(Eq. 2)}$$

The specific surface area (S_{BET}) was selected as the response variable, and the experimental data were analyzed using Minitab Statistical Software, version 17.1.0.

2.3. Synthesis of Au-Ag nanoparticles supported on biochar

For catalyst synthesis, 500 mg of biochar (BC) was dispersed in 10 mL of ultrapure water and magnetically stirred for 10 min. Gold and silver precursor solutions were subsequently added at different Ag-to-Au molar ratios, as detailed in Table S1. The monometallic condition corresponded to 188 μmol of metal precursor; therefore, for the bimetallic systems, the total amount of the two metal precursors was kept at 188 μmol. After precursor addition, the suspension was stirred for an additional 10 min.

An aqueous $NaBH_4$ solution (0.0564 mol L^{-1}, 20 mL) was subsequently added. The mixture was magnetically stirred for 10 min at room temperature and subsequently heated at a controlled temperature of 70 °C for 20 min under continuous magnetic stirring. At the end of the reaction, the material was washed three times with deionized water, with centrifugation performed after each washing step. The resulting solid was subsequently dried in an oven at 60 °C for 12 h.

2.4. Biochar characterization

Elemental analysis (C, H, N, and S) was performed using a LECO TruSpec Micro analyzer. Oxygen content was estimated by difference, subtracting the sum of the other elements from 100%.

Specific surface area (S_{BET}) was determined using an N_2 physisorption analyzer (NOVA 600, Anton Paar). Before measurements, the samples were degassed at 120 °C for 4 h. N_2 adsorption was then performed at 120 °C for 4 h, and S_{BET} was calculated using the Brunauer–Emmett–Teller (BET) method.

Surface morphology was analyzed by scanning electron microscopy (SEM) using a FIB-Quanta FEG 3D FEI microscope (FEI Company, USA) coupled to an energy-dispersive X-ray spectroscopy (EDS) system for qualitative elemental analysis.

High-resolution transmission electron microscopy (HRTEM) was performed using a Tecnai G2-20 FEI SuperTwin microscope operated at 200 kV and equipped with an energy-dispersive X-ray spectroscopy (EDS) detector. Samples were dispersed in water, and an aliquot was deposited onto copper grids. EDS analysis was performed using a silicon drift detector with an energy resolution of 133 eV.

Surface functional groups were evaluated by Fourier-transform infrared spectroscopy (FTIR) using an ALPHA II spectrometer (Bruker, USA) equipped with an attenuated total reflectance (ATR) accessory. Measurements were acquired over 16 scans in the 400–4000 cm^{-1} range at a resolution of 4 cm^{-1}.

X-ray diffraction (XRD) patterns were recorded using a Bruker D8 Discover diffractometer equipped with a copper X-ray tube and a Göbel mirror.

The point of zero charge (pH_{PZC}) was determined using the pH-drift method in a KCl electrolyte solution (0.100 mol L^{-1}), following a procedure adapted from (de Souza et al., 2024). Erlenmeyer flasks containing 20 mg of material and 20.00 mL of KCl solution (0.100 mol L^{-1}) were prepared, and the initial pH was adjusted to values between 2 and 12 using HCl or NaOH solutions, both at 0.100 mol L^{-1}. The samples were maintained under agitation at 200 rpm for 24 h at approximately 25 °C. The final pH was subsequently measured, and the pH_{PZC} was determined from the intersection of the plot of ($pH_{final} - pH_{initial}$) versus $pH_{initial}$ with the zero line (y = 0). All measurements were performed in duplicate.

Surface acidic functional groups were quantified by Boehm titration (Barbosa et al., 2014). For this purpose, three separate assays were conducted, each consisting of 100 mg of material added to 25 mL of either $NaHCO_3$, Na_2CO_3, or NaOH solution (0.100 mol L^{-1}). Each suspension was maintained under agitation at 180 rpm for 24 h at 25 °C. After filtration, aliquots of the supernatant were titrated with standardized HCl solution (0.100 mol L^{-1}) using phenolphthalein as the indicator. Blank assays were performed to correct the results. Carboxylic, lactonic, and phenolic groups were quantified based on the differential consumption of the reagents, as presented in Eq. 3–5, respectively.

$$[COOH] = \frac{n_{NaHCO_3}}{m} \quad \text{Eq. 3}$$

$$[Lactone] = \frac{n_{Na_2CO_3} - n_{NaHCO_3}}{m} \quad \text{Eq. 4}$$

$$[Phenol] = \frac{n_{NaOH} - n_{Na_2CO_3}}{m} \quad \text{Eq. 5}$$

2.5. Nitrophenol reduction

The p-NP reduction reaction was conducted directly in a quartz cuvette at ambient temperature and pressure and monitored by UV–Vis spectrophotometry. The catalytic activity of the different Au-Ag NPs/BC-OT compositions were evaluated, including $Au_{0.75}$-$Ag_{0.25}$ NPs/BC-OT, $Au_{0.5}$-$Ag_{0.5}$ NPs/BC-OT and $Au_{0.25}$-$Ag_{0.75}$ NPs/BC-OT. Initially, 3.0 mg of catalyst was dispersed in 3.0 mL of ultrapure water, followed by the addition of 150 µL of p-NP solution (0.80 mmol L^{-1}), after which the reaction was monitored spectrophotometrically over the wavelength range of 100–1200 nm. The resulting apparent rate constants (k_{app}) were used to compare the catalytic performance of the materials.

The reaction progress was monitored by UV–Vis spectrophotometry at predetermined times (30, 90, 180, 300, and 420 s), with manual agitation between

measurements to ensure adequate homogenization of the reaction suspension. The reaction kinetics were evaluated using a pseudo-first-order model with respect to p-NP, considering the excess of $NaBH_4$. Under these conditions, the $NaBH_4$ concentration can be assumed to remain approximately constant throughout the reaction and is therefore incorporated into the apparent rate constant (k_{app}).

The apparent rate constant was determined from the linear relationship between $\ln(A_0/A_t)$ and reaction time, where A_0 and A_t represent the absorbance of p-NP at 400 nm at the initial time and at a given reaction time, respectively. Because p-NP concentration was monitored indirectly by UV–Vis spectrophotometry, the absorbance at 400 nm was used for the kinetic analysis. According to the Beer–Lambert law, absorbance is directly proportional to p-NP concentration. Thus, the pseudo-first-order rate expression can be expressed in terms of absorbance, as given in Equation 6. The slope of the resulting linear plot corresponds to the apparent rate constant (k_{app}).

$$\ln\left(\frac{A_0}{A_t}\right) = -k_{app}t \qquad \text{Eq. 6}$$

2.6. Control experiments

To compare the catalytic activity of the different materials, reduction assays were also performed using BC-OT without nanoparticles, Ag NPs/BC-OT, Au NPs/BC-OT, unsupported $Au_{0.5}$-$Ag_{0.5}$ NPs, $ZnCl_2$, ZnO, under the same reaction conditions.

2.7. Reuse of $Au_{0.5}$-$Ag_{0.5}$ NPs/BC-OT

To evaluate catalyst stability and reusability, successive p-NP reduction cycles were performed under the same experimental conditions described above. At the end of each cycle, the catalyst was recovered by centrifugation at 4000 rpm for 5 min. The recovered material was then stirred in 10 mL of NaOH solution (0.1 mol L^{-1}) for 30 min

and washed twice with Milli-Q water. The washed material was subsequently reused in a new catalytic cycle under the same experimental conditions.

3. RESULTS AND DISCUSSION

3.1. Optimization of passion fruit peel-derived biochar synthesis

The pyrolysis yields, final yields after washing, and specific surface areas of the $ZnCl_2$-activated passion fruit peel biochars are presented in Table S2. Pyrolysis yields ranged from 69.3 to 83.9%, reflecting the mass of the pyrolyzed solids, including retained $ZnCl_2$, whereas final yields after washing ranged from 32.4 to 67.0%, following the removal of soluble $ZnCl_2$ and other soluble species. The observed variations in yield are associated with mass losses during pyrolysis, mainly due to the release of volatile compounds, and during subsequent washing, primarily due to the removal of soluble inorganic species (Netto et al., 2025a). The final process yields obtained in this work are within the range reported for biochars derived from other lignocellulosic and biomass feedstocks. (Ali et al., 2025) reported a yield of 39.63% for pine sawdust-derived biochar produced at 500 °C. Similarly, (Senthilkumar et al., 2026) obtained yields ranging from 38.25 to 42.55% for biochars derived from the invasive brown alga *Sargassum siliquosum* over the temperature range of 400-800 °C.

Specific surface area was selected as the response variable because higher surface areas provide greater accessibility and availability of surface sites for nanoparticle deposition, favoring the development of biochar-supported catalysts. Analysis of variance (ANOVA) was performed on the data, and the results are presented in Table S3. The quadratic model for the $ZnCl_2$-activated biochar was statistically significant ($p < 0.05$), and the corresponding fitted equation is presented in Equation 7.

$$AS = -32061 + 100.5\,T + 138.9\,t + 2755\,IR - 0.0844\,T^*T - 0.375\,t^*t - 237.4\,IR^*IR - 0.1309\,T^*t - 1.96\,T^*IR - 12.66\,t^*IR \quad \text{(Equation 7)}$$

Here, ***AS*** represents specific surface area, ***T*** represents carbonization temperature, ***t*** represents residence time, and ***IR*** represents impregnation ratio.

The significant model terms were the linear and quadratic effects of temperature, the quadratic effect of impregnation ratio, and the linear interaction between residence time and impregnation ratio. The coefficients of determination, R^2 (93.76%) and adjusted R^2 (86.74%), indicate that the model explains a substantial proportion of the variability in specific surface area. In addition, the lack-of-fit test was not significant ($p > 0.05$), indicating no statistical evidence of lack of fit and supporting the adequacy of the model for describing the response. This model was used to optimize the process parameters and guide the production of biochar under optimized conditions.

The Pareto chart of standardized effects is presented in Figure S1. Temperature, in its linear term, had the largest absolute standardized effect (7.48), indicating that it was the most influential factor within the experimental domain. The quadratic terms of temperature and impregnation ratio were also statistically significant ($p < 0.05$), indicating nonlinear effects and suggesting the presence of optimum conditions within the studied ranges. The interaction between residence time and impregnation ratio was statistically significant, indicating that the effect of impregnation ratio on the response depends on residence time. In contrast, residence time showed a lower overall contribution to the response. Its linear and quadratic terms were not statistically significant, whereas its interaction with impregnation ratio was significant. Overall, these results are consistent with the ANOVA findings described above. The response surfaces presented in Figure 1 show the combined effects of the variables on specific surface area

(S_{BET}). Overall, all variables showed parabolic behavior, with maximum S_{BET} values at intermediate conditions within the evaluated ranges. Pyrolysis temperature and impregnation ratio had more pronounced effects on the response, whereas residence time showed a less pronounced effect, consistent with the ANOVA results, in which only its interaction with impregnation ratio was significant. These results indicate the existence of optimum synthesis conditions for maximizing the specific surface area of the biochar.

The desirability analysis (Figure S2) indicated that the estimated conditions for maximizing specific surface area (S_{BET}) were approximately 525 °C, 60 min, and an impregnation ratio of 2.0, resulting in a predicted value of approximately 1278 m^2 g^{-1}. The prediction profiles confirmed the nonlinear behavior of temperature and impregnation ratio, with well-defined maxima, whereas residence time showed a less pronounced effect over the experimental range. Based on these results, these conditions were selected for the synthesis of the optimized biochar, designated BC-OT.

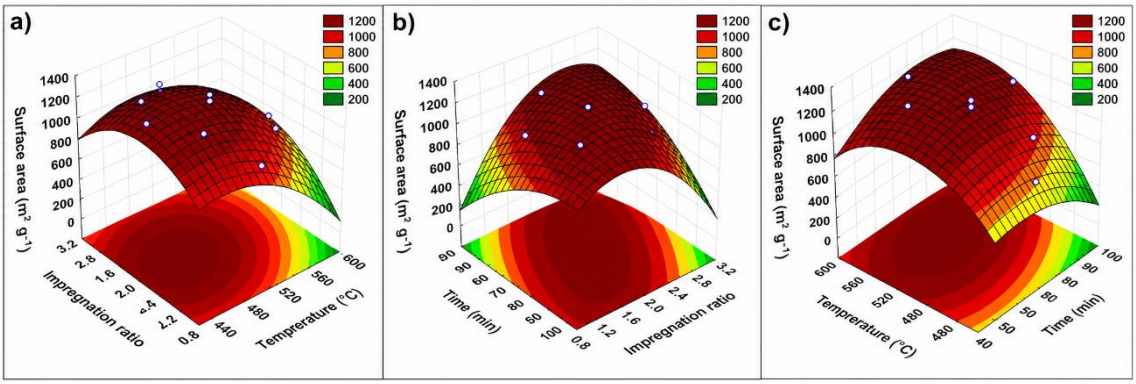


Figure 1. Response surface plots for the specific surface area (S_{BET}) of passion fruit peel-derived biochar obtained using a Central Composite Rotatable Design: (a) temperature × impregnation ratio; (b) time × impregnation ratio; and (c) temperature × time.

The biochar produced under the optimized conditions (BC-OT) exhibited an experimental specific surface area of 1411.64 m^2 g^{-1}, which was 9.43% higher than the value predicted by the model. The close agreement between the experimental and predicted values confirms the adequacy of the optimization, while the higher

experimental value indicates that BC-OT achieved a specific surface area slightly above that estimated by the model, consistent with its well-developed porous structure.

3.2.Characterization of biochars

BC-OT was characterized using a comprehensive set of analytical techniques to assess its physicochemical and textural characteristics. The elemental composition is presented in Table 2. BC-OT showed a substantial increase in carbon content and a decrease in hydrogen content relative to the precursor biomass, reflecting the effects of pyrolysis and the progressive removal of volatile constituents. The decrease in oxygen content further indicates extensive devolatilization and carbonization, resulting in enrichment of the carbon fraction and increased carbonization of the material (Netto et al., 2025a).

Table 2. Elemental analysis (% w w^{-1}) and atomic H/C and O/C ratios of passion fruit peel biomass and optimized $ZnCl_2$-activated biochar (BC-OT).

Material	C (% w w^{-1})	H (% w w^{-1})	N (% w w^{-1})	S (% w w^{-1})	O (% w w^{-1})	H/C	O/C
Biomass	41.654	5.676	2.347	ND	50.323	1.624	0.907
BC-OT	63.419	1.801	2.153	0.400	32.227	0.338	0.381

ND = Not detected.

The atomic H/C ratio decreased after pyrolysis, suggesting increased aromaticity and a higher degree of structural condensation in the biochar (Netto et al., 2025a; Netto et al., 2025b). This behavior is associated with the degradation of aliphatic structures and formation of more thermally stable carbonaceous arrangements (Netto et al., 2025a). Additionally, the decrease in the O/C ratio indicates a reduction in oxygen-containing functional groups on the material surface (Netto et al., 2025b). The O/C value obtained for BC-OT (0.381) was below 0.60, a parameter frequently used as an indicator of biochar environmental stability. Materials within this range have been reported to exhibit

intermediate half-lives, estimated at 100–1000 years (Netto et al., 2025a; Rabichi et al., 2024). These characteristics suggest desirable chemical stability for applications requiring reuse and preservation of structural properties over time. According to European Biochar Certificate (EBC) criteria, molar O/C ratios below 0.4 indicate biochars with medium stability (Rabichi et al., 2024). A similar trend was observed by Netto et al. (2025b), who reported reductions in H/C from 1.79 to 0.79 and 1.02, and in O/C from 0.75 to 0.71 and 0.64, for biochars produced from pulp industry sludge activated with H_3PO_4 and KOH, respectively. In another study, decreases in H/C and O/C ratios were observed for phosphoric-acid-activated biochars pyrolyzed at 450 and 500 °C (Netto et al., 2025a).

The N_2 adsorption–desorption isotherms of the biomass and BC-OT are shown in Figure 2. Both materials exhibited type IV isotherms according to the IUPAC (International Union of Pure and Applied Chemistry) classification (Thommes et al., 2015), indicating the predominance of mesopores in the biochars (dos Santos Silva et al., 2024).

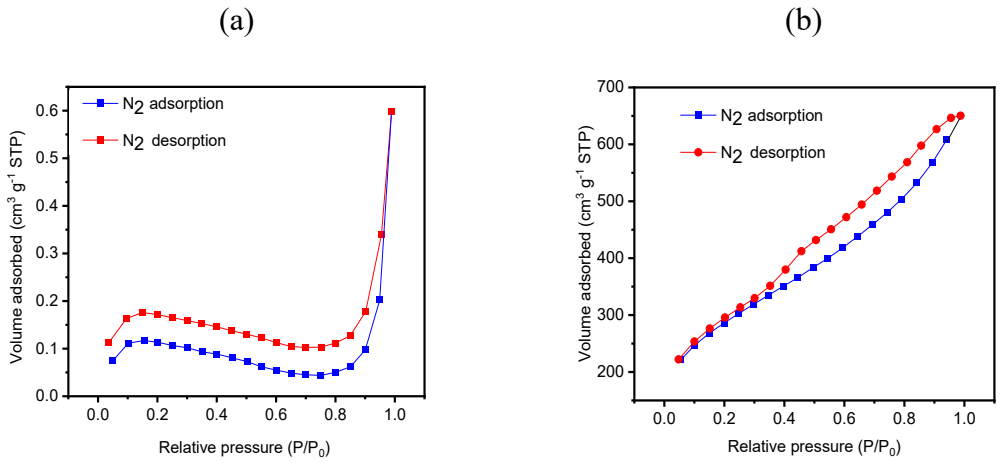


Figure 2. N_2 adsorption–desorption isotherms of (a) passion fruit peel biomass and (b) optimized $ZnCl_2$-activated biochar (BC-OT).

The precursor biomass, Figure 2(a), exhibited a weak hysteresis loop, suggesting low accessible porosity and limited structural development. In contrast, BC-OT, Figure

2(b), exhibited a more pronounced hysteresis loop, indicating greater development of the mesoporous structure and a significant increase in specific surface area after chemical activation (Thommes et al., 2015). The specific surface areas of the biomass and BC-OT (Table S4) were 0.257 and 1411.64 m^2 g^{-1}, respectively. The pronounced increase in specific surface area after $ZnCl_2$ chemical activation confirms the effectiveness of the process in developing porosity. Similar behavior has been reported in the literature. Chen *et al*. (2023) obtained specific surface areas of 12.7 and 111.0 m^2 g^{-1} for passion fruit waste biomass and activated biochar, respectively (Chen et al., 2023). Although the authors used H_3PO_4 as the activating agent, the present results indicate that $ZnCl_2$ is also highly effective in developing the porous structure.

Pore volume increased substantially after chemical activation and pyrolysis, from 0.0004 cm^3 g^{-1} for the biomass to 0.6905 cm^3 g^{-1} for BC-OT. This increase indicates the development of a more accessible porous structure, favoring molecular diffusion into the material and contributing to the increase in specific surface area. Peres *et al*. (2024) reported a pore volume of 0.03 cm^3 g^{-1} for biochar produced from passion fruit waste activated with $K_2C_2O_4$ (Peres et al., 2024). In contrast, the value for BC-OT falls within the range reported for $ZnCl_2$-activated biochars derived from other lignocellulosic biomasses (0.38-0.69 cm^3 g^{-1}), demonstrating the high effectiveness of the activating agent in pore development (Michael & Surya, 2024). In addition, the mean pore diameters of the biomass and BC-OT were 17.58 and 3.46 nm, respectively. BC-OT can be classified as a mesoporous material because its pores are within the 2–50 nm range (Thommes et al., 2015). Similar results were reported by Chen *et al*. (2023), who obtained a pore diameter of 3.21 nm for activated biochar derived from passion fruit waste.

The biomass and BC-OT were analyzed by SEM, and the results are presented in Figure 3. The biomass exhibited a fibrous structure with preserved fibers, whereas BC-

OT showed a rougher lamellar-fibrous structure, with cavities, pores, and fissures formed because of pyrolysis.

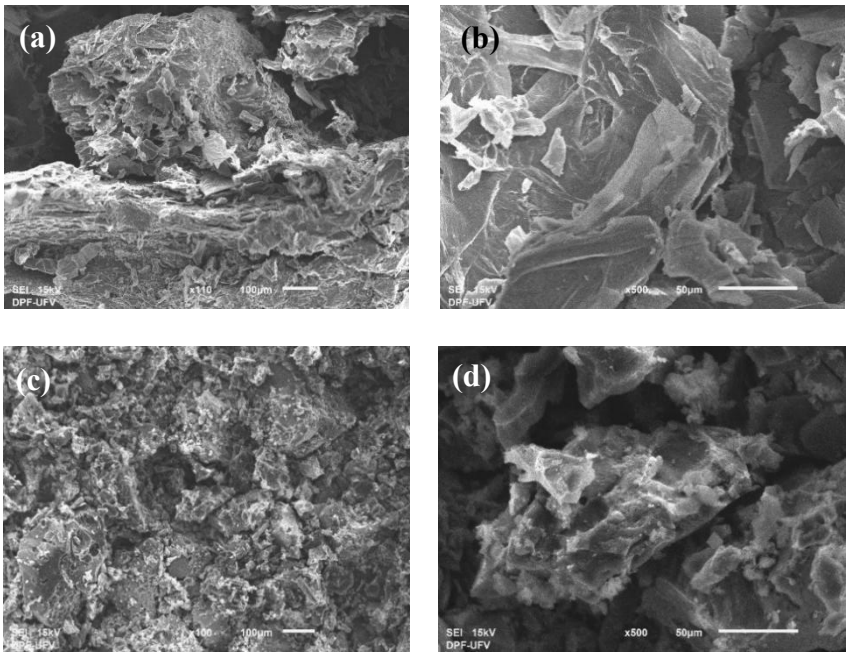


Figure 3. Scanning electron microscopy (SEM) images of passion fruit peel biomass and optimized $ZnCl_2$-activated biochar (BC-OT): (a-b) biomass and (c-d) BC-OT.

The EDS spectra are presented in Figure S3. The EDS spectra indicated a predominance of carbon in both materials. In the passion fruit peel biomass, oxygen and potassium signals were also observed, with potassium associated with the natural mineral composition of passion fruit residues (Peres et al., 2024; Salgado et al., 2010). After activation and carbonization, zinc and chlorine were detected in addition to carbon and oxygen, attributable to the use of $ZnCl_2$ as the chemical activating agent (Netto et al., 2026). The chemical maps in Figure S4(a–d) showed that carbon, oxygen, and potassium were distributed throughout the material, with lower intensity for potassium. The elemental distribution maps for BC-OT [Figure S4(e–i)] revealed a homogeneous carbon distribution throughout the matrix, alongside localized regions enriched in O, Zn, and Cl.

The FTIR spectra of the biomass and BC-OT are shown in Figure S5. The biomass exhibited bands characteristic of lignocellulosic materials. In the 3200–3600 cm^{-1} region,

O–H stretching appeared as a broad and intense band in the biomass spectrum and with reduced intensity in BC-OT, indicating a decrease in hydroxyl groups after pyrolysis (dos Santos Silva et al., 2024). In the biomass, aliphatic C–H stretching was observed at 2923 and 2847 cm^{-1} (dos Santos Silva et al., 2024). At approximately 1731 cm^{-1}, a band assigned to C=O stretching was observed in the biomass spectrum (dos Santos Silva et al., 2024). Around 1594 cm^{-1}, aromatic C=C stretching was observed in both materials, indicating the presence of condensed aromatic structures (dos Santos Silva et al., 2024). An intense absorption band near 1010 cm^{-1} was attributed to C–O and C–O–C stretching vibrations, being particularly prominent in the raw biomass (Netto et al., 2025a). After pyrolysis, band intensities decreased and oxygen-containing functional groups were reduced, accompanied by an increase in material aromaticity. These results corroborate the CHNS/O, SEM, and S_{BET} analyses, particularly regarding the formation of a more porous, carbonized material with greater aromatic character.

The X-ray diffraction (XRD) patterns of the biomass and BC-OT are presented in Figure S6. Overall, both materials exhibited a broad peak in the 2θ range of 15–30°, indicating a predominantly amorphous nature associated with disordered carbon structures (Netto et al., 2026). The BC-OT diffractogram showed peaks at 31.7°, 34.4°, 36.2°, 47.5°, 56.6°, and 62.8° (2θ), which are in good agreement with the crystallographic pattern of hexagonal wurtzite ZnO (JCPDS 36-1451) (Figure S6). Its presence is consistent with $ZnCl_2$ chemical activation (Zhang et al., 2024) and the EDS results showing zinc on the material surface. The formation or persistence of zinc-containing mineral species on the material surface may contribute to biochar surface properties, affecting its reactivity, stability, and behavior (Bhakta et al., 2023).

In addition to the peaks assigned to ZnO, a low-intensity reflection at approximately 64.5° was observed in both the biomass and BC-OT. The persistence of

this signal after pyrolysis and washing to neutral pH suggests an association with intrinsic mineral constituents of the biomass, possibly related to the plant ash fraction (Tomczyk et al., 2020). Considering the EDS results for the biomass, which showed potassium and oxygen, this reflection may be associated with minerals containing these elements. However, unambiguous identification of the crystalline structure responsible for this peak was not possible using XRD and EDS data alone; complementary analyses are required to confirm the crystalline compound present in the biomass.

The pH_{PZC} value of BC-OT was determined as 6.53 from the intersection of the ΔpH curve with the ΔpH = 0 line (Figure S7a). Thus, the surfaces tend to be positively charged below its respective pH_{PZC} values and negatively charged above it (Netto et al., 2025b). Boehm titration indicated a predominance of lactonic groups on the BC-OT surface, with a concentration of 1.50 mmol g^{-1}. The absence of the characteristic lactone band in the FTIR spectrum (1730–1750 cm^{-1}), despite the positive Boehm titration result, may be attributed to the low concentration of these groups on the biochar surface (J. Chen et al., 2024). This discrepancy reflects differences in the sensitivity of the techniques, with Boehm titration being more suitable for detecting low concentrations of surface functional groups in biochar (Luo et al., 2024). Carboxylic and phenolic groups were not detected by the methodology used, which may be related to their low surface density resulting from carbonization and the influence of inorganic constituents such as mineral ash and metal oxides (Netto et al., 2025). The presence of zinc- and potassium-containing species detected by XRD and EDS suggests that these inorganic constituents may participate in the titration and contribute to the observed results. In addition, the pH_{PZC} of 6.53, close to neutrality, indicates a low density of acidic groups on the BC-OT surface (Wu et al., 2026).

Dynamic light scattering (DLS) analysis of the $Au_{0.5}$-$Ag_{0.5}$ NPs/BC-OT suspension showed a hydrodynamic diameter of 232 nm and a polydispersity index (PDI) of 0.10 (Figure 4). This hydrodynamic diameter is considerably larger than the average nanoparticle diameter determined by HRTEM (7.4 ± 3.4 nm), as DLS measures the effective hydrodynamic size of dispersed entities, which includes the solvation layer and may also reflect the presence of associated particles or aggregates. Similar behavior has been reported for bimetallic Ag–Au nanoparticles, with a hydrodynamic diameter of 150.88 nm and a PDI of 0.13 determined by DLS (Kumari et al., 2025). Therefore, the DLS result should be interpreted as the hydrodynamic size of the dispersed Au–Ag/BC-OT entities rather than the primary size of individual metallic nanoparticles (Filippov et al., 2023). The zeta potential was −21.99 mV, indicating a negatively charged surface of the dispersed entities.

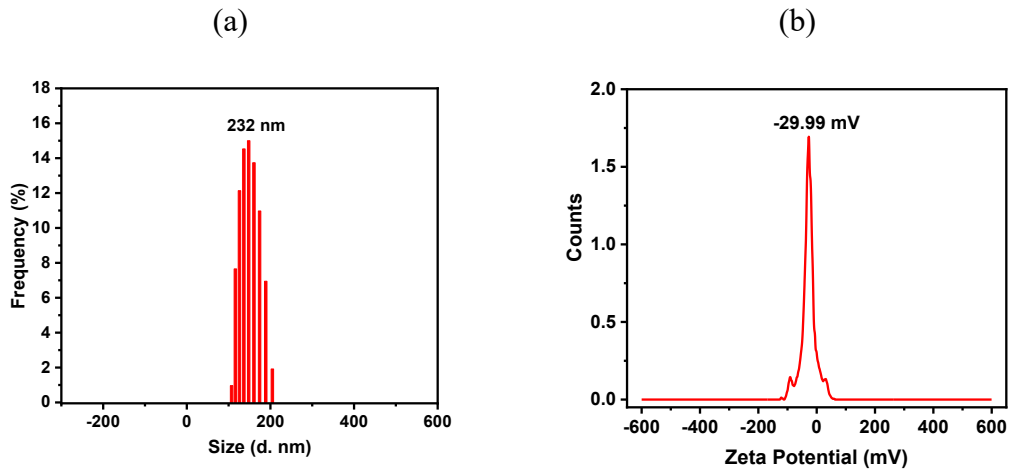


Figure 4. (a) Hydrodynamic size distribution determined by dynamic light scattering (DLS) and (b) Zeta potential of $Ag_{0.5}$-$Au_{0.5}$ NPs/BC-OT.

Characterization of BC-OT indicated that $ZnCl_2$ activation and pyrolysis produced a porous carbonaceous matrix with suitable surface characteristics for metal incorporation. Based on these properties, BC-OT was used as support for Au and Ag nanoparticles to evaluate their catalytic performance in p-NP reduction.

3.3. Characterization of $Au_{0.5}$-$Ag_{0.5}$ NPs/BC-OT catalyst

The optimized biochar was used as a support for Au and Ag nanoparticles ($Au_{0.5}$-$Ag_{0.5}$ NPs/BC-OT) to develop heterogeneous catalysts for the reduction of p-NP to p-AP using $NaBH_4$ as the reducing agent. The $Au_{0.5}$-$Ag_{0.5}$ NPs/BC-OT catalyst exhibited a pH_{PZC} of 7.60. The higher pH_{PZC} suggests a less acidic surface after nanoparticle incorporation, with surface charge influenced by the carbonaceous structure and mineral species remaining after chemical activation and carbonization (Zhao et al., 2015).

Figure 5(a) shows the HRTEM morphology, revealing the carbonaceous matrix and regions with a higher particle concentration. At higher magnification, spherical particles of different sizes distributed over the support and regions of agglomeration can be observed [Figure 5(b)]. Figure 5(c) shows a representative micrograph used for particle-size determination, together with the size-distribution histogram. A total of 186 particles with individually resolved contours were analyzed, yielding an average diameter of 7.4 ± 3.4 nm. Similar results were reported by (Dworzak et al., 2024). The HRTEM images revealed lattice fringes associated with crystalline domains, as shown in Figure 5(d), with experimental interplanar spacings (**d_{exp}**) of approximately 0.237, 0.205, 0.253, 0.262, and 0.279 nm, as presented in Table S5. The values of 0.237 and 0.205 nm were compatible with the (111) and (200) planes, respectively, of a face-centered cubic (fcc) structure associated with metallic Au and/or Ag (Negri et al., 2024). Because the lattice parameters of the two metals are similar, the observed domains could not be assigned unambiguously to Au, Ag, or structures containing both elements based solely on interplanar spacings (Dworzak et al., 2024). The spacings of approximately 0.262 and 0.279 nm were consistent with the (002) and (100) planes, respectively, of wurtzite ZnO (Bui et al., 2024). The 0.253 nm spacing was also close to the reference value for the (101) plane. However, this assignment remains tentative because of the deviation from

the reference value, uncertainty in manually determining the fringe positions, and the measurement of only one crystalline domain (Cherkashin et al., 2023).

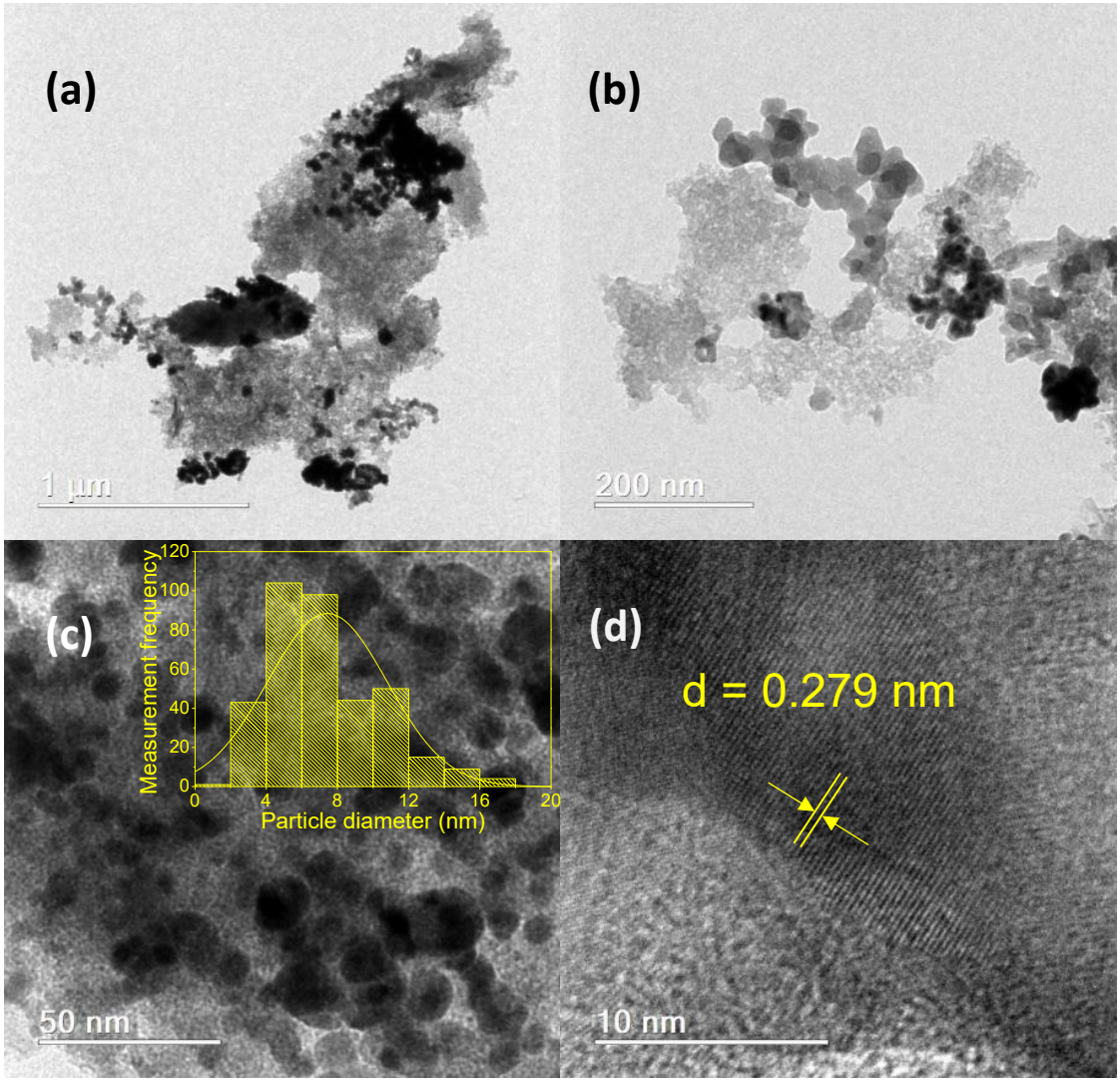


Figure 5. HRTEM characterization of $Au_{0.5}$-$Ag_{0.5}$ NPs/BC-OT: (a–b) representative micrographs; (c) particle-size distribution histogram; and (d) lattice fringes.

EDS coupled to HRTEM (Figure S8) also confirmed the simultaneous presence of Ag and Au in $Au_{0.5}$-$Ag_{0.5}$ NPs/BC-OT. The presence of Zn is attributable to chemical activation with $ZnCl_2$ (Li et al., 2023). The dominant carbon signal originated from the carbonaceous BC-OT matrix, whereas the intense Cu signal arose from the copper grid used for HRTEM sample preparation (Ede et al., 2026). The oxygen signal may be attributed to oxygen-containing functional groups in the carbonaceous matrix and inorganic oxygen-containing species, particularly ZnO (An et al., 2024). S and P were

detected at low concentrations and may be attributed to the natural composition of the biomass (dos Reis et al., 2018), whereas Cl is associated with the $ZnCl_2$ activation process.

The SAED pattern showed five rings corresponding to distinct interplanar spacings (Figure S9 and Table S6). Spacings of approximately 0.236, 0.202, 0.145, and 0.123 nm were consistent with the (111), (200), (220), and (311) planes, respectively, of the face-centered cubic structure of metallic Ag and/or Au (Dworzak et al., 2024). The 0.145 nm spacing may include contributions from both the (220) plane of Au/Ag and the (103) plane of ZnO (Dworzak et al., 2024; Kang et al., 2025). The proximity of these interplanar spacings and the potential overlap of diffraction contributions in the SAED pattern preclude an unambiguous assignment of the crystalline phases based solely on interplanar spacings. The ring at 0.326 nm is consistent with the (002) plane of graphitic carbon (Guo et al., 2024).

The fcc structure assignment was further assessed using the diffraction-vector magnitudes (***g***), calculated from the corresponding interplanar spacings (***d***) according to Eq. 8. The experimental g-ratios were then compared with the theoretical ratios expected for an fcc structure, providing an additional criterion for phase assignment.

$$g = \frac{1}{d} \qquad \text{Eq. 8}$$

For interplanar spacings of 0.236, 0.202, 0.145, and 0.123 nm, the corresponding ***g*** values were 4.237, 4.950, 6.897, and 8.130 nm^{-1}, respectively (Table S7). Normalization to the first ring gave experimental ratios of 1.000, 1.168, 1.628, and 1.919, compared with theoretical ratios of 1.000, 1.155, 1.633, and 1.915 for the (111), (200), (220), and (311) planes of an fcc structure, respectively. The deviations of less than 2% support the

assignment of these rings to the corresponding planes of an fcc crystalline domain (Dworzak et al., 2024; Weirich, 2024).

3.4. Application of $Au_{0.5}$-$Ag_{0.5}$ NPs/BC-OT in the catalytic reduction of p-nitrophenol

The catalytic activity of the nanocomposites was evaluated using the reduction of p-nitrophenol, with the effects of the experimental parameters on catalytic performance investigated. Figure 6(a) shows the UV–Vis absorption spectra of the starting compound (p-nitrophenol) and the target product (p-aminophenol). Upon addition of $NaBH_4$, the p-nitrophenol absorption band shifted from 318 to approximately 400 nm, consistent with the formation of p-nitrophenolate under alkaline conditions. The appearance of the characteristic p-aminophenol band at 298 nm enabled spectrophotometric monitoring of the conversion of p-nitrophenol to p-aminophenol.

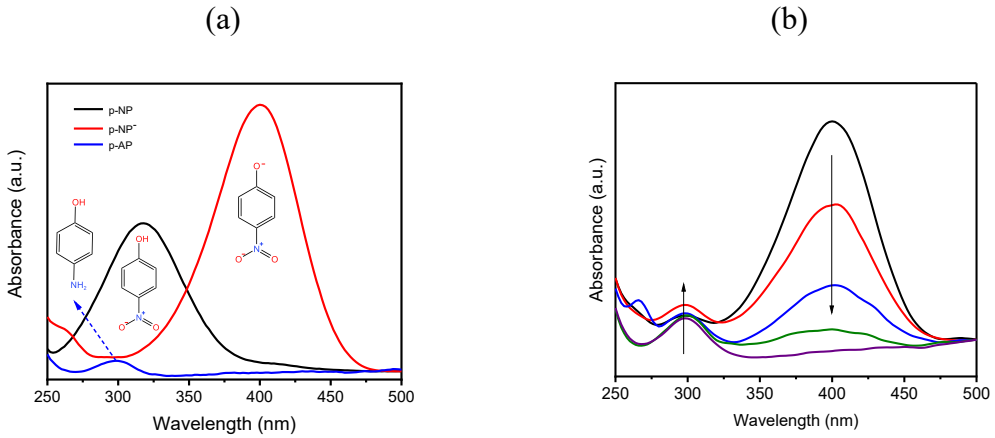


Figure 6. UV–Vis absorption spectra of p-nitrophenol (p-NP) and p-aminophenol (p-AP): (a) reference spectra and reaction mixture after 7 min in the presence of $Au_{0.5}$-$Ag_{0.5}$ NPs/BC-OT; and (b) time evolution of the UV–Vis spectra during p-NP reduction by $NaBH_4$ catalyzed by $Au_{0.5}$-$Ag_{0.5}$ NPs/BC-OT. Reaction conditions: 3 mg of catalyst, [p-NP] = 36.4 µmol L^{-1}, [$NaBH_4$] = 3633.3 µmol L^{-1}, room temperature (~25 °C), and reaction time = 7 min.

Catalyst doses of 3, 6, and 10 mg of $Au_{0.5}$-$Ag_{0.5}$ NPs/BC-OT were evaluated under otherwise identical conditions (Figure S10). Increasing the catalyst dose altered the band intensities and spectral baseline, likely due to increased light scattering by the suspended

catalyst particles (Alidoust Ghatar et al., 2024). Therefore, the apparent decrease in the 400 nm band, assigned to p-nitrophenolate formed under alkaline conditions in the presence of $NaBH_4$ (Rathee et al., 2023), at higher catalyst doses should not be interpreted as evidence of greater p-NP conversion, as it may instead result from increased light scattering by the suspended catalyst particles (Alidoust Ghatar et al., 2024). Suspensions containing 3 and 6 mg yielded better-defined spectra, whereas 10 mg produced greater optical interference, hindering spectral interpretation. Therefore, 3 mg was selected for subsequent experiments because it minimized the contribution of support to the spectral signal and allowed more reliable monitoring of changes in p-NP concentration over time.

Different Au/Ag ratios supported on BC-OT were evaluated for catalytic p-NP reduction in the presence of $NaBH_4$. Figure 6(b) presents the time evolution of the spectra obtained for $Ag_{0.5}$-$Au_{0.5}$ NPs/BC-OT, corresponding to the central composition used in the screening study (Table S1) to evaluate the influence of Au/Ag ratios on the catalytic activity of the synthesized materials. A progressive decrease in the band centered at 400 nm, assigned to the p-nitrophenolate ion ($p\text{-}NP^-$) formed under alkaline conditions in the presence of $NaBH_4$ (Rathee et al., 2023), was observed. Simultaneously, a band near 300 nm appeared, consistent with p-AP formation through reduction of the nitro group ($-NO_2$) to an amino group ($-NH_2$) (Hamad et al., 2025).

Comparison of supported and unsupported systems allows the contribution of the carbonaceous matrix to be distinguished from that of the metal species. Based on the temporal change in absorbance at 400 nm, apparent rate constants (k_{app}) were calculated for the synthesized materials (Table S8), enabling quantitative comparison of their catalytic activities [Figure 7(a)]. BC-OT exhibited a k_{app} of $(1.11 \pm 0.21) \times 10^{-3}$ s^{-1}, whereas unsupported Ag and Au exhibited only $(0.10 \pm 0.06) \times 10^{-3}$ s^{-1} and $(0.03 \pm 0.01) \times 10^{-3}$ s^{-1}, respectively. The unsupported Ag–Au system also showed low activity, (0.03 ±

0.02) × 10^{-3} s^{-1}, indicating that the metals alone were insufficient to produce high activity under the evaluated conditions. In contrast, nanoparticle deposition on BC-OT increased activity, particularly for the bimetallic system. $Ag_{0.5}$-$Au_{0.5}$ NPs/BC-OT showed the highest mean k_{app}, (15.18 ± 2.27) × 10^{-3} s^{-1}, followed by $Ag_{0.75}$-$Au_{0.25}$ NPs/BC-OT, with (10.96 ± 0.78) × 10^{-3} s^{-1}. The marked increase in activity for the bimetallic systems suggests a synergistic effect between Au and Ag nanoparticles. Interaction between the two metals may promote electronic redistribution at the catalytic surface, facilitating electron transfer from the reducing agent ($NaBH_4$) to p-NP and accelerating its conversion to p-AP (Eduardo et al., 2024; Lyu et al., 2023).

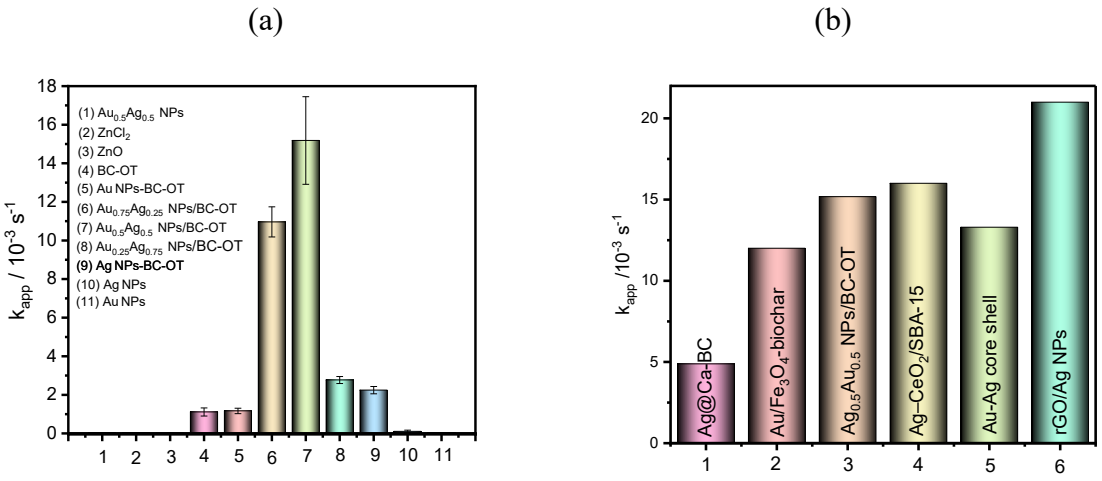


Figure 7. Catalytic performance for p-nitrophenol reduction: (a) apparent rate constants (k_{app}) obtained for the synthesized catalysts and control materials, reaction conditions [p-NP] = 36.4 µmol L^{-1} and [$NaBH_4$] = 3633.3 µmol L^{-1}; and (b) comparison of the catalytic performance of $Au_{0.5}$-$Ag_{0.5}$ NPs/BC-OT with literature-reported catalysts. References: (1) Jacob et al. (2024); (2) Lopes et al. (2021); (3) this work; (4) Taratayko et al. (2021); (5) (Mejía and Bogireddy, 2022); (6) Sun et al. (2023).

The contribution of Zn-containing species was also evaluated using $ZnCl_2$ and ZnO controls, which exhibited k_{app} values of (0.02 ± 0.02) × 10^{-3} s^{-1} and (0.01 ± 0.01) × 10^{-3} s^{-1}, respectively. These values are lower than that of BC-OT and, particularly, the Ag- and Au-containing catalysts, indicating that Zn species associated with activation are not, by themselves, the main source of the observed catalytic activity. Although Zn may

contribute to support surface characteristics, the kinetic results indicate a predominant synergistic contribution from the carbonaceous matrix combined with Ag and Au species in p-NP reduction. Because $Au_{0.5}$-$Ag_{0.5}$ NPs/BC-OT showed the best performance, it was selected for subsequent reuse studies.

The $Au_{0.5}$-$Ag_{0.5}$ NPs/BC-OT catalyst exhibited an apparent rate constant of (15.18 ± 2.27) × 10^{-3} s^{-1}. This value is comparable to those reported for other nanocatalysts in the $NaBH_4$-mediated reduction of p-nitrophenol [Figure 7(b)]. Reported values include 16.0 × 10^{-3} s^{-1} for Ag–CeO_2/SBA-15 (Taratayko et al., 2021), (12.0 ± 2.0) × 10^{-3} s^{-1} for Au nanoparticles supported on magnetized biochar (Lopes et al., 2021), and 21.0 × 10^{-3} s^{-1} for Ag nanoparticles on reduced graphene oxide (Sun et al., 2023). Lower values were reported for Ag nanoparticles supported on calcite-rich biochar (4.88 × 10^{-3} s^{-1}) (Jacob et al., 2024) and Au–Ag core–shell systems (13.3 × 10^{-3} s^{-1}) (Mejía and Bogireddy, 2022) (Figure 6b). These results indicate comparable catalytic performance. The catalyst also uses support derived from passion fruit peel waste.

Catalyst reuse was evaluated over four consecutive p-NP reduction cycles (Figure S11). The k_{app} × 1000 values were 10.66, 7.81, 6.23, and 5.67 s^{-1} for the first, second, third, and fourth cycles, respectively. A progressive decrease in the apparent rate constant was observed. This decrease may be associated with partial loss of metal nanoparticles or catalyst material during recovery and washing (Li et al., 2023). Nanoparticle aggregation may also contribute to the loss of activity (Dworzak et al., 2024). In addition, adsorbed species may block active sites during the reaction (Shakor & Al-Shafei, 2023). Despite the decrease in activity, $Au_{0.5}$-$Ag_{0.5}$ NPs/BC-OT maintained catalytic activity after four consecutive cycles. The results indicate that the catalyst can be recovered and reused for at least four cycles.

Despite the decrease in k_{app}, the spectra obtained in the fourth cycle (Figure S12) retained the characteristic reaction profile. The band at 400 nm, assigned to the p-nitrophenolate ion, decreased during the reaction. A new absorption band near 300 nm, associated with p-aminophenol formation, also appeared. These spectral changes indicate that the catalyst remained active after successive recovery and washing steps. Although the apparent reaction rate decreased over the cycles, the $Au_{0.5}$-$Ag_{0.5}$ NPs/BC-OT catalyst retained its catalytic activity.

3.5 Proposed catalytic cycle

Based on the characterization and kinetic results and considering the mechanism proposed by Li and Chen (2013), a catalytic cycle is proposed (Figure 8). BH_4^- ions are adsorbed on the $Au_{0.5}Ag_{0.5}$ NPs, where their activation facilitates electron transfer to the catalytic surface. Simultaneously, p-nitrophenolate is adsorbed at the available active sites. Its adsorption can be favored by both the metal nanoparticles and the BC-OT support, which provides a high surface area, a mesoporous structure, and oxygen-containing functional groups. The biochar support also promotes nanoparticle dispersion and may facilitate electron transfer between BH_4^-, the $Au_{0.5}$-$Ag_{0.5}$ NPs, and adsorbed p-nitrophenolate. The $Au_{0.5}$-$Ag_{0.5}$ NPs/BC-OT interface may further facilitate electron migration and accumulation, favoring charge transfer to the nitro group. The reduction of the nitro group can proceed through sequential steps involving nitroso (–NO) and hydroxylamine (–NHOH) intermediates. Further reduction leads to the formation of p-aminophenol, which is subsequently desorbed from the catalyst surface. Overall, the proposed cycle involves adsorption of the reactants, electron transfer, sequential reduction of the nitro group, and desorption of the product (Elbayoumy et al., 2025; M. Li & Chen, 2013; Strachan et al., 2020).

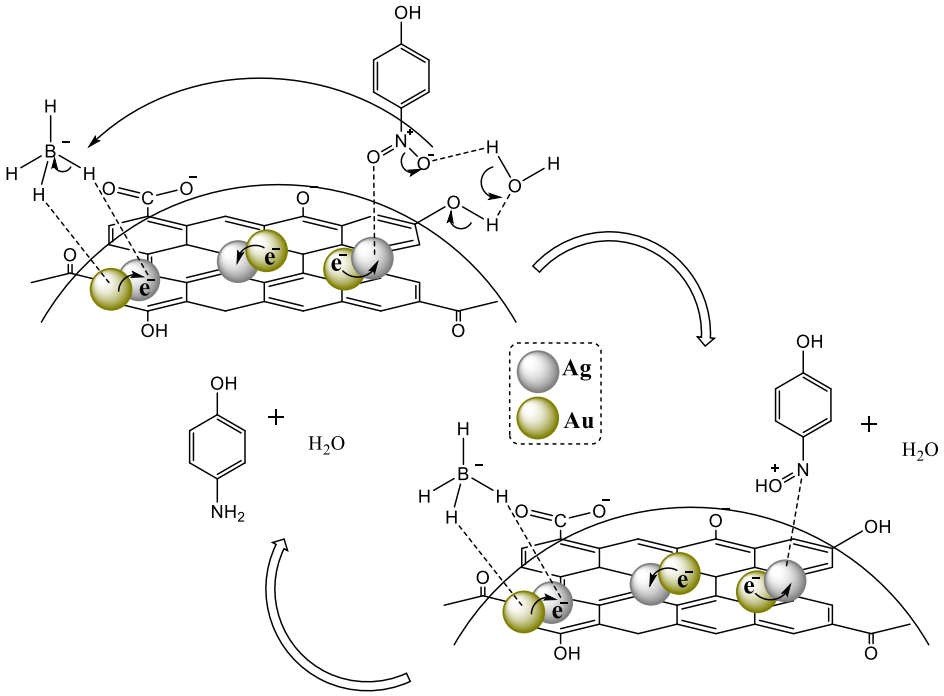


Figure 8. Schematic representation of the proposed mechanism for p-nitrophenol reduction to p-aminophenol by $NaBH_4$ mediated by $Au_{0.5}$-$Ag_{0.5}$ NPs/BC-OT.

EDS, HRTEM, and SAED analyses confirmed the presence of Au and Ag in the catalyst, as well as nanoscale particles and crystalline domains consistent with an fcc structure of metallic Au and Ag. These results support the involvement of metallic surfaces in catalytic reactions. In the bimetallic system, the Au-Ag interface may influence the electronic structure and adsorption of the reactants. These effects may facilitate electron transfer to the nitro group and weaken the N–O bonds, thereby favoring the reduction of p-nitrophenolate to p-aminophenol (Eduardo et al., 2024).

4. CONCLUSIONS

The Central Composite Rotatable Design was suitable for evaluating the effects of carbonization temperature, residence time, and impregnation ratio on the specific surface area of passion fruit peel-derived biochar. The multivariate approach enabled the identification of suitable synthesis conditions while reducing the number of experiments and promoting more efficient use of time and reagents. Characterization techniques

demonstrated that $ZnCl_2$ chemical activation and pyrolysis promoted carbon enrichment, increased aromatic character, formation of cavities and fissures, and development of a predominantly mesoporous structure with high specific surface area. BC-OT also exhibited a surface character close to neutrality and the presence of lactonic groups. Functionalization of BC-OT with Au and Ag resulted in active catalysts for p-nitrophenol reduction by $NaBH_4$. HRTEM, EDS, and SAED analyses revealed nanoscale particles distributed over the carbonaceous matrix, with a heterogeneous size distribution and regions of agglomeration. Au and Ag were identified, together with domains compatible with a face-centered cubic structure. Among the evaluated materials, $Au_{0.5}$-$Ag_{0.5}$ NPs/BC-OT showed the best catalytic performance, outperforming the monometallic materials and the non-functionalized support. The catalyst remained active over four consecutive reuse cycles, although the apparent reaction rate decreased progressively. Thus, the proposed objectives were achieved, demonstrating the feasibility of passion fruit peel as a precursor for a high-surface-area carbonaceous support and its application in the development of heterogeneous catalysts for the reduction of nitroaromatic compounds.

Statements & Declarations

Funding: This research was financially supported by the Brazilian Federal Agency for Support and Evaluation of Graduate Education (CAPES), the National Council for Scientific and Technological Development (CNPq; Grants 407799/2022-2, 405828/2022-5, and 305608/2025-8), and the Research Support Foundation of the State of Minas Gerais (FAPEMIG; Grants APQ-03572-23, RED-00144-22, and APQ-00834-26).

Competing Interests: The authors declare that they have no competing interests.

Statement on the Use of AI-Assisted Technologies: During manuscript preparation, AI-assisted tools, including ChatGPT, were used solely to improve grammar, language, and

overall writing clarity. The authors retain full responsibility for all scientific content, technical interpretations, and conclusions presented in the manuscript.

Author Contributions: Daliane Cláudia de Faria: Investigation, data curation, formal analysis, and writing—original draft. Antonio Machado Netto: Investigation, data curation, and formal analysis. Igor Pecly Estephaneli: Investigation, methodology, and formal analysis. Ana Luíza Quintão Santos: Investigation and data curation. Fernanda Bicalho Almeida Papa: Investigation and formal analysis. Frederico Garcia Pinto: Methodology, supervision, and writing—review and editing. Renata Pereira Lopes Moreira: Conceptualization, methodology, supervision, project administration, funding acquisition, and writing—review and editing. All authors contributed to the interpretation of the results, reviewed the manuscript, and approved the final version.

Acknowledgments: The authors gratefully acknowledge financial support from the Brazilian Federal Agency for Support and Evaluation of Graduate Education (CAPES), the National Council for Scientific and Technological Development (CNPq; Grants 407799/2022-2, 405828/2022-5, and 305608/2025-8), and the Research Support Foundation of the State of Minas Gerais (FAPEMIG; Grants APQ-03572-23, RED-00144-22 and APQ-00834-26). The authors also acknowledge the Departments of Chemistry and Physics at the Federal University of Viçosa for technical support and the Center of Microscopy at the Federal University of Minas Gerais for access to its facilities.

Data Availability: The data sets generated and/or analyzed during the current study are not publicly available but are available from the corresponding author on reasonable request.

References

Ali, M., Mahmood, F., Magoua Mbeugang, C. F., Tang, J., Xie, X., & Li, B. (2025). Molten chloride salt pyrolysis of biomass: Effects of temperature and mass ratio of

molten salt to biomass. *Energy*, *316*, 134634. https://doi.org/10.1016/J.ENERGY.2025.134634

Alidoust Ghatar, A., Auguié, B., & Le Ru, E. C. (2024). Forward-Scattering and Multiple-Scattering Sources of Errors in UV–Visible Spectroscopy of Microspheres. *Analytical Chemistry*, *96*(49), 19723–19731. https://doi.org/10.1021/ACS.ANALCHEM.4C04912

An, Z., Sánchez-Montes, I., Chelme-Ayala, P., Chen, C., & Gamal El-Din, M. (2024). Efficient degradation of naphthenic acids in water using a sustainable engineered biochar/ZnO composite under simulated solar light. *Chemical Engineering Journal*, *489*, 151308. https://doi.org/10.1016/j.cej.2024.151308

Aslam, J., Waseem, M. A., Lu, X. M., Sun, W., & Wang, Y. (2025). From biochar to battery electrodes: A pathway to green lithium and sodium-ion battery systems. *Chemical Engineering Journal*, *505*, 159556. https://doi.org/10.1016/J.CEJ.2025.159556

Atinafu, D. G., Choi, J. Y., Nam, J., Kang, Y., & Kim, S. (2025). Insights into the effects of biomass feedstock and pyrolysis conditions on the energy storage capacity and durability of standard biochar-based phase-change composites. *Biochar*, *7*(1), 18-. https://doi.org/10.1007/S42773-024-00396-1

Badamasi, H., Naeem, Z., Antoniolli, G., Praveen Kumar, A., Olaleye, A. A., Sadiq, I. S., Durimin-iya, N. I., & Khan, M. S. (2025). A review of recent advances in green and sustainable technologies for removing 4-nitrophenol from the water and wastewater. *Sustainable Chemistry and Pharmacy*, *43*, 101867. https://doi.org/10.1016/J.SCP.2024.101867

Barbosa, C. S., Santana, S. A. A., Bezerra, C. W. B., & Silva, H. A. D. S. (2014). Remoção de compostos fenólicos de soluções aquosas utilizando carvão ativado preparado a partir do aguapé (eichhornia crassipes): Estudo cinético e de equilíbrio termodinâmico. *Quimica Nova*, *37*(3), 447–453. https://doi.org/10.5935/0100-4042.20140066

Bhakta, A. K., Tang, M., Snoussi, Y., Khalil, A. M., Mascarenhas, R. J., Mekhalif, Z., Abderrabba, M., Ammar, S., & Chehimi, M. M. (2023). Sweety, salty, sour, and romantic biochar-supported ZnO: highly active composite catalysts for environmental remediation. *Emergent Materials 2023 8:4*, *8*(4), 2647–2661. https://doi.org/10.1007/S42247-023-00599-5

Bui, T. S., Ma, Z., Yuwono, J. A., Kumar, P. V., O'Connell, G. E. P., Peng, L., Yang, Y., Lim, M., Daiyan, R., Lovell, E. C., & Amal, R. (2024). Enhanced Nitrate-to-Ammonia Activity on Fe/ZnO Nanoparticles via Tuning Intermediate Adsorption in Alkaline Electrolyte. *Advanced Functional Materials*, *34*(48), 2408704. https://doi.org/10.1002/ADFM.202408704

Cabral, L. L., Bottini, R. C. R., Gonçalves, A. J., Junior, M. M., Rizzo-Domingues, R. C. P., Lenzi, M. K., Nagalli, A., Passig, F. H., dos Santos, P. M., & de Carvalho, K. Q. (2025). Food dye adsorption in single and ternary systems by the novel passion

fruit peel biochar adsorbent. *Food Chemistry*, *464*, 141592. https://doi.org/10.1016/J.FOODCHEM.2024.141592

Chandravanshi, R., Tiwari, A., Tiwari, A., Dubey, R., & Pandey, S. K. (2026). Biochar as an adsorbent for microplastics present in aquatic environments: A comparative review between batch and column adsorption. *Journal of Environmental Chemical Engineering*, *14*(3), 122530. https://doi.org/10.1016/J.JECE.2026.122530

Chen, B. J., Yang, L., Sun, Y., Zhong, S., Liang, G., Sun, Y., Jiang, T., Li, X., Zhou, L., & Khoo, H. E. (2023). Structural Characterization of Activated Carbon Prepared from Passion Fruit By-Product for Removal of Cholesterol and Toxic Compound in Liquid Food. *Journal of Biobased Materials and Bioenergy*, *17*(2), 232–244. https://doi.org/10.1166/JBMB.2023.2265

Chen, J., Zhou, J., Zheng, W., Leng, S., Ai, Z., Zhang, W., Yang, Z., Yang, J., Xu, Z., Cao, J., Zhang, M., Leng, L., & Li, H. (2024). A complete review on the oxygen-containing functional groups of biochar: Formation mechanisms, detection methods, engineering, and applications. *Science of The Total Environment*, *946*, 174081. https://doi.org/10.1016/J.SCITOTENV.2024.174081

Cheng, H. W., Bonnet, S., & Gheewala, S. H. (2026). Life cycle assessment of bamboo residue management pathways: Biochar and alternatives for carbon sequestration and circular economy. *Sustainable Production and Consumption*, *63*, 86–102. https://doi.org/10.1016/J.SPC.2026.01.004

Cherkashin, N., Louiset, A., Chmielewski, A., Kim, D. J., Dubourdieu, C., & Schamm-Chardon, S. (2023). Quantitative mapping of strain and displacement fields over HR-TEM and HR-STEM images of crystals with reference to a virtual lattice. *Ultramicroscopy*, *253*, 113778. https://doi.org/10.1016/J.ULTRAMIC.2023.113778

de Almeida, L. S., Teixeira, F. R. P., Moreira, C. de A., Nascimento, J. C. N., de Albuquerque, L. A., Roselino, M. N., Assis, J. L. de J., Reis, R. C., Jesus, O. N. de, Dias, F. de S., & Fricks, A. T. (2026). High-Intensity Ultrasound Processing of Passion Fruit Pulp: Effects on Physicochemical Properties, Microbiological Quality, Bioactive Compound Retention, and Ascorbate Oxidase Activity. *Foods 2026, Vol. 15, 15*(7). https://doi.org/10.3390/FOODS15071187

de Souza, N. C. S., do Carmo Dias, G., Puiatti, G. A., de Oliveira, K. L. A., Vitorino, T. B., Silva, T. A., & Moreira, R. P. L. (2024). Eco-Friendly Photodegradation of Direct Red 80 Dye Mediated by Biochar Decorated with Cobalt Ferrite. *International Journal of Environmental Science and Technology 2024 22:6*, *22*(6), 4263–4280. https://doi.org/10.1007/S13762-024-05883-3

dos Reis, L. C. R., Facco, E. M. P., Salvador, M., Flôres, S. H., & de Oliveira Rios, A. (2018). Antioxidant potential and physicochemical characterization of yellow, purple and orange passion fruit. *Journal of Food Science and Technology*, *55*(7), 2679. https://doi.org/10.1007/S13197-018-3190-2

dos Santos Silva, A. A., Bousada, G. M., Mazzini, L. F. M., Guezguan, S. M., de Freitas, C. P. M., Monteiro, K. A., dos Santos Renato, N., & Moreira, R. P. L. (2024). Biochar from malt residue: Toward a circular economy for sustainable

fluoroquinolone removal in aqueous systems. *Journal of Analytical and Applied Pyrolysis*, *183*, 106707. https://doi.org/10.1016/J.JAAP.2024.106707

Dworzak, A., Paciok, P., Mahr, C., Heggen, M., Dosche, C., Rosenauer, A., & Oezaslan, M. (2024). Tuning the morphology and chemical distribution of Ag atoms in Au rich nanoparticles using electrochemical dealloying. *Nanoscale*, *16*(19), 9603–9616. https://doi.org/10.1039/D4NR00046C

Ede, S. R., Paige, H. M., Wu, J., Adhikari, C. M., Kumbhar, A. S., Han, S., & Luo, Z. (2026). Computational–experimental assessment of transition-metal doping of Co 3 O 4 for acidic oxygen evolution reaction with balanced activity and stability. *Journal of Materials Chemistry A*, *14*(6), 3297–3307. https://doi.org/10.1039/D5TA08166A

Eduardo, S. B., El Hachimi, A. G., Monge, M., López-de-Luzuriaga, J. M., Agarwal, V., & Bogireddy, N. K. R. (2024). Na+ and Cl− adsorption derived enhancement in 4-nitrophenol reduction using Au/Ag nanoparticle: An experimental and theoretical study. *Chemosphere*, *367*, 143576. https://doi.org/10.1016/J.CHEMOSPHERE.2024.143576

Elbayoumy, E., El-Bindary, A. A., Nakano, T., & Aboelnga, M. M. (2025). Silver nanoparticles immobilized on crosslinked vinyl polymer for catalytic reduction of nitrophenol: experimental and computational studies. *Scientific Reports*, *15*(1), 717-. https://doi.org/10.1038/s41598-024-82183-3

Escalante, J. J., Chen, W. H., Su, C. Y., Li, P. H., Lin, K. Y. A., & Manatura, K. (2026). Statistical optimization of biochar production via high-temperature carbonization through Taguchi and principal component analysis approaches. *Fuel*, *410*, 137846. https://doi.org/10.1016/J.FUEL.2025.137846

Fan, B., Zhou, L., Xing, L., & Zhang, W. (2025). Fabricating cellulose nanocrystals from passion fruit peel to enhance the properties of electrospun zein/poly(ethylene oxide) nanofibrous films. *Food Hydrocolloids*, *166*, 111355. https://doi.org/10.1016/J.FOODHYD.2025.111355

Filippov, S. K., Khusnutdinov, R., Murmiliuk, A., Inam, W., Zakharova, L. Y., Zhang, H., & Khutoryanskiy, V. V. (2023). Dynamic light scattering and transmission electron microscopy in drug delivery: a roadmap for correct characterization of nanoparticles and interpretation of results. *Materials Horizons*, *10*(12), 5354–5370. https://doi.org/10.1039/D3MH00717K

Guo, Z., Papineau, D., O'Neil, J., Rizo, H., Chen, Z. Q., Qiu, X., & She, Z. (2024). Abiotic synthesis of graphitic carbons in the Eoarchean Saglek-Hebron metasedimentary rocks. *Nature Communications 2024 15:1*, *15*(1), 5679-. https://doi.org/10.1038/s41467-024-50134-1

Hamad, N., Galhoum, A. A., Saad, A., & Wageh, S. (2025). Efficient catalytic reduction of methylene blue and p-Nitrophenol by CuNP/hydrochar nanocomposites synthesized from organic peel waste. *Scientific Reports 2025 15:1*, *15*(1), 24996-. https://doi.org/10.1038/s41598-025-08360-0

Jacob, J. A. E., Antony, R., & Jebakumar, D. S. I. (2024). Synergistic effect of silver nanoparticle-embedded calcite-rich biochar derived from Tamarindus indica bark on 4-nitrophenol reduction. *Chemosphere*, *349*, 140765. https://doi.org/10.1016/J.CHEMOSPHERE.2023.140765

Kang, I., Kim, S., Lee, S. M., Jeong, S. H., Ki, H. J., Lee, U. J., Ko, J. H., Son, B. J., Kim, S., & Kang, J. (2025). ZnO electrocatalyst integrated onto carbon paper for efficient non-aqueous Li–O2 batteries. *RSC Advances*, *15*(35), 28348–28357. https://doi.org/10.1039/D5RA03545G

Kumari, S., Rohilla, R., Rani, S., & Prabhakar, N. (2025). Tagetes erecta synthesized bimetallic Ag–Au nanoparticles and their potential application in electrochemical detection and estimation of ampicillin in raw milk. *RSC Advances*, *15*(27), 21528–21540. https://doi.org/10.1039/D5RA03037D

Lavorato, J. A., de Oliveira Brahim Cortez, M., Dalmolin da Silva, M., Netto, A. M., Louzada, L. N., Silva de Souza, N. C., do Nascimento Rodrigues, L., da Silva, R. C., de Moura Guimarães, L., Astruc, D., & Moreira, R. P. L. (2026). Pequi Seed Biochar as Pd Nanoparticle Support for Catalytic Hydrogen Evolution from Ammonia Borane. *ACS Omega*, *11*(27), 39775–39787. https://doi.org/10.1021/ACSOMEGA.5C13606

Li, B., Li, C., Li, D., Zhang, L., Zhang, S., Cui, Z., Wang, D., Tang, Y., & Hu, X. (2023). Activation of pine needles with zinc chloride: Evolution of functionalities and structures of activated carbon versus increasing temperature. *Fuel Processing Technology*, *252*, 107987. https://doi.org/10.1016/J.FUPROC.2023.107987

Li, D., Liu, T., Luo, Y., Zhuge, X., Luo, K., Luo, Z., Liu, X., & Zhang, K. (2023). Reversible ligand exchange of triphenylphosphine with thiols on gold nanoparticles for Janus modification and catalyst recycling. *Separation and Purification Technology*, *322*, 124154. https://doi.org/10.1016/J.SEPPUR.2023.124154

Li, M., & Chen, G. (2013). Revisiting catalytic model reaction p-nitrophenol/NaBH4 using metallic nanoparticles coated on polymeric spheres. *Nanoscale*, *5*(23), 11919–11927. https://doi.org/10.1039/C3NR03521B

Lobo, W. V., Paes, O. A. R. L., Sousa, A. dos S., Pinheiro, W., Sousa, C. A. S., de Araújo Bezerra, J., Novita, L., Cheng, I. F., de Souza, L. K. C., & de Freitas, F. A. (2025). Application of sulfonated passion fruit seeds as a heterogeneous catalyst in the esterification of oleic and levulinic acids: Optimization of reaction parameters. *Renewable Energy*, *241*, 122355. https://doi.org/10.1016/J.RENENE.2025.122355

Lopes, R. P., Guimarães, T., & Astruc, D. (2021). Magnetized biochar as a gold nanocatalyst support for p-nitrophenol reduction. *Journal of the Brazilian Chemical Society*, *32*(8), 1680–1686. https://doi.org/10.21577/0103-5053.20210056

Luo, Q., Deng, Y., Li, Y., He, Q., Wu, H., & Fang, X. (2024). Effects of pyrolysis temperatures on the structural properties of straw biochar and its adsorption of tris-

(1-chloro-2-propyl) phosphate. *Scientific Reports 2024 14:1*, *14*(1), 25711-. https://doi.org/10.1038/s41598-024-77299-5

Lyu, X., Liu, Q., Yuan, Q., Liang, X., Chen, Q., Luo, P., Yang, Y., Fang, Z., & Bao, H. (2023). Ultrafast synthesis of multi-branched Au/Ag bimetallic nanoparticles at room temperature for photothermal reduction of 4-nitrophenol. *Journal of Catalysis*, *428*, 115174. https://doi.org/10.1016/J.JCAT.2023.115174

Mejía, Y. R., & Bogireddy, N. K. R. (2022). Reduction of 4-nitrophenol using green-fabricated metal nanoparticles. *RSC Advances*, *12*(29), 18661–18675. https://doi.org/10.1039/D2RA02663E

Michael, M. S., & Surya, K. (2024). Feasibility study on conversion of biowaste of lemon peel into carbon electrode for supercapacitor using ZnCl2 as an activating agent. *Materials for Renewable and Sustainable Energy*, *13*(3), 409–420. https://doi.org/10.1007/S40243-024-00273-8

Morim, A. C., Madaleno, M., Tarelho, L. A. C., & Silva, F. C. (2025). Financial feasibility of biochar production: A comparative analysis of business scenarios. *Journal of Cleaner Production*, *536*, 147167. https://doi.org/10.1016/J.JCLEPRO.2025.147167

Negri, C., Colombo, R., Bracconi, M., Atzori, C., Donazzi, A., Lucotti, A., Tommasini, M., & Maestri, M. (2024). Operando UV-vis spectroscopy for real-time monitoring of nanoparticle size in reaction conditions: a case study on rWGS over Au nanoparticles. *Catalysis Science & Technology*, *14*(5), 1318–1327. https://doi.org/10.1039/D3CY01392H

Netto, A. M., da Silva, M. D., de Oliveira Brahim Cortez, M., Dias, G. do C., de Souza, B. F., Bousada, G. M., & Moreira, R. P. L. (2026). Platinum-decorated biochar from pequi tree bark as a sustainable catalyst for hydrogen production from ammonia borane. *Carbon Letters 2026*, 1–16. https://doi.org/10.1007/S42823-026-01084-9

Netto, A. M., De Oliveira, M., Cortez, B., Pedro, J., Ferreira, R., Chagas Da Silva, R., Rodrigues, L. N., De Moura, L., Es, G., Pereira, R., & Moreira, L. (2026). Sustainable Conversion of Pulp Industry Sludge into Activated Biochar for High-Performance Methylene Blue Removal. *ACS Omega*, *11*(6), 9497–9509. https://doi.org/10.1021/acsomega.5c09623

Netto, A. M., Nascimento, M. C. G. M., de Caux, L. S., Cortez, M. de O. B., Ferreira, J. P. R., Monteiro, K. A., & Moreira, R. P. L. (2025). Tertiary Treatment of Pulp Industry Effluents Using Activated Biochar Derived from Biological Sludge Within a Circular Economy Framework. *Processes 2025, Vol. 13, 13*(6). https://doi.org/10.3390/PR13061647

Netto, A. M., Pedro, J., Ferreira, R., Monteiro, K. A., De Lima, C. S., Varejão, J. O. S., Vinicius, E., Varejão, V., Renato, N. S., & Moreira, R. P. L. (2025). Optimization of Biochar Synthesis from Cosmetic Industry Sludge for Enhanced Removal of Enrofloxacin. *J. Braz. Chem. Soc. 2025*, *36*, 1–12. https://doi.org/10.21577/0103-5053.20250097

OECD-FAO. (2023). OECD-FAO Agricultural Outlook 2023-2032. In *OECD Agriculture Statistics*. OECD Publishing. https://doi.org/10.1787/AGR-OUTL-DATA-EN

Osire, N. G., & Gnaro, M. A. (2026). Optimization of sugarcane bagasse biochar based Sulphonated solid acid catalyst synthesis using Response surface methodology. *Results in Engineering*, 110658. https://doi.org/10.1016/J.RINENG.2026.110658

Peres, C. B., Morais, L. C. de, & Resende, P. M. R. (2024). Carbon adsorption on waste biomass of passion fruit peel: A promising machine learning model for CO2 capture. *Journal of CO2 Utilization*, *80*, 102680. https://doi.org/10.1016/J.JCOU.2024.102680

Rabichi, I., Sekkouri, C., Yaacoubi, F. E., Ennaciri, K., Izghri, Z., Bouzid, T., El Fels, L., & Baçaoui, A. (2024). Experimental and Theoretical Investigation of Olive Mill Solid Waste Biochar for Vanillic Acid Adsorption Using DFT/B3LYP Analysis. *Water, Air, & Soil Pollution 2024 235:6*, *235*(6), 369-. https://doi.org/10.1007/S11270-024-07183-5

Rathee, G., Chugh, H., Kohli, S., Gaur, R. K., & Chandra, R. (2023). Exploring the catalytic degradation of 4-nitrophenol and in vitro cytotoxicity of gold nanoparticle-doped NiAlTi LDH. *Materials Advances*, *4*(7), 1656–1663. https://doi.org/10.1039/D2MA01081J

Salgado, J. M., Bombarde, T. A. D., Mansi, D. N., Piedade, S. M. de S., & Meletti, L. M. M. (2010). Effects of different concentrations of passion fruit peel (Passiflora edulis) on the glicemic control in diabetic rat. *Food Science and Technology*, *30*(3), 784–789. https://doi.org/10.1590/S0101-20612010000300034

Samghouli, N., Bencheikh, I., Azoulay, K., Jansson, S., & El Hajjaji, S. (2025). Mechanistic and reactional activation study of carbons destined for emerging pharmaceutical pollutant adsorption. *Environmental Monitoring and Assessment 2025 197:3*, *197*(3), 259-. https://doi.org/10.1007/S10661-025-13685-4

Sands, R. (Ronald D.), Meade, B., Seale, J. L., Robinson, S., & Seeger, R. (2023). Scenarios of global food consumption Scenarios of Global Food Consumption: Implications for Agriculture. *Economic Research Service USDA*. https://doi.org/10.32747/2023.8134356.ERS

Senthilkumar, G., Nagarajan, D., Chen, L., Chen, C. W., Chang, J. S., & Dong, C. Di. (2026). Valorization of invasive brown seaweed Sargassum: ZnCl2-Activated biochar for efficient azo dye removal. *Biomass and Bioenergy*, *210*, 109070. https://doi.org/10.1016/J.BIOMBIOE.2026.109070

Shakor, Z. M., & Al-Shafei, E. N. (2023). The mathematical catalyst deactivation models: a mini review. *RSC Advances*, *13*(32), 22579–22592. https://doi.org/10.1039/D3RA02912C

Sharma, S., Sharma, U., Sharma, N., Rana, V. S., Thakur, S., Kumar, A., & Kumar, R. (2025). Exploring the valorization of fruit bio-waste for sustainable utilization in

agro-food industries: A Comprehensive Review. *Food Bioscience*, *63*, 105768. https://doi.org/10.1016/J.FBIO.2024.105768

Skjennum, K. A., Mulder, J., Breedveld, G. D., Hartnik, T., Estoppey, N., & Sørmo, E. (2026). Long-term efficiency of biochar amendment in PFAS-contaminated soil under unsaturated field conditions. *Journal of Hazardous Materials*, *510*, 142119. https://doi.org/10.1016/J.JHAZMAT.2026.142119

Strachan, J., Barnett, C., Masters, A. F., & Maschmeyer, T. (2020). 4-Nitrophenol Reduction: Probing the Putative Mechanism of the Model Reaction. *ACS Catalysis*, *10*(10), 5516–5521. https://doi.org/10.1021/ACSCATAL.0C00725

Sun, W., Hong, Y., Li, T., Chu, H., Liu, J., Feng, L., & Baghayeri, M. (2023). Biogenic synthesis of reduced graphene oxide decorated with silver nanoparticles (rGO/Ag NPs) using table olive (olea europaea) for efficient and rapid catalytic reduction of organic pollutants. *Chemosphere*, *310*, 136759. https://doi.org/10.1016/J.CHEMOSPHERE.2022.136759

Sun, X., Ma, Y., Pang, L., Wei, J., Fu, H., Li, Y., Li, Y., Lu, J., & Bao, M. (2025). Enhancement of petroleum degradation by biochar supported Fe3O4 nanoparticles: Role of immobilized Rhodococcus hoagii S4 in oil spill remediation. *Journal of Hazardous Materials*, *496*, 139333. https://doi.org/10.1016/J.JHAZMAT.2025.139333

Taratayko, A., Larichev, Y., Zaikovskii, V., Mikheeva, N., & Mamontov, G. (2021). Ag–CeO2/SBA-15 composite prepared from Pluronic P123@SBA-15 hybrid as catalyst for room-temperature reduction of 4-nitrophenol. *Catalysis Today*, *375*, 576–584. https://doi.org/10.1016/J.CATTOD.2020.05.001

Thommes, M., Kaneko, K., Neimark, A. V., Olivier, J. P., Rodriguez-Reinoso, F., Rouquerol, J., & Sing, K. S. W. (2015). Physisorption of gases, with special reference to the evaluation of surface area and pore size distribution (IUPAC Technical Report). *Pure and Applied Chemistry*, *87*(9–10), 1051–1069. https://doi.org/10.1515/PAC-2014-1117/XML

Tomczyk, A., Sokołowska, Z., & Boguta, P. (2020). Biochar physicochemical properties: pyrolysis temperature and feedstock kind effects. *Reviews in Environmental Science and Bio/Technology 2020 19:1*, *19*(1), 191–215. https://doi.org/10.1007/S11157-020-09523-3

UNITED NATIONS. (2015). *Transforming our world: the 2030 agenda for sustainable development.* A/RES/70/1. New York.

Weirich, T. E. (2024). A simple protocol for determining the zone axis direction from selected-area electron diffraction spot patterns of cubic materials. *Journal of Applied Crystallography*, *57*(4), 1263–1269. https://doi.org/10.1107/S1600576724004333

Wu, R., Zhang, M., Adnan, F. H., Siow, P. Y., & Abidin, M. I. I. Z. (2026). Biochar-Based Approaches for Heavy Metal Remediation in Agricultural Soils:

Mechanisms, Optimization, and Emerging AI Applications. *BioResources* , *21*(3). https://doi.org/10.15376/BIORES.21.3.WU

Wu, Y., Zhang, H., Wei, Z., Xiong, D., Bai, S., Tong, M., & Ma, P. (2023). Structure and Catalytic Performance of Carbon-Based Solid Acids from Biomass Activated by ZnCl2. *Catalysts 2023, Vol. 13, 13*(11). https://doi.org/10.3390/CATAL13111436

Zhang, H., Wei, Z., Xiong, D., Wu, Y., Tong, M., Su, H., Zhang, Z., & Liao, J. (2024). Investigation into the Structure and Properties of Biochar Co-Activated by ZnCl2 and NaHCO3 under Low Temperature Conditions. *Materials 2024, Vol. 17, 17*(4). https://doi.org/10.3390/MA17040942

Zhao, L., Cao, X., Zheng, W., Wang, Q., & Yang, F. (2015). Endogenous minerals have influences on surface electrochemistry and ion exchange properties of biochar. *Chemosphere*, *136*, 133–139. https://doi.org/10.1016/J.CHEMOSPHERE.2015.04.053

Zhou, Z., Li, H., Rao, T., Wang, C., Du, J., Huang, J., & Xu, S. (2024). Efficient degradation of ciprofloxacin by peroxymonosulfate activated with Co-loaded waste biomass: Efficiency, stability, and mechanism. *Journal of Environmental Chemical Engineering*, *12*(6), 114810. https://doi.org/10.1016/J.JECE.2024.114810

Zhu, G., Zhu, M., Wang, E., Gong, C., Wang, Y., Guo, W., Xie, G., Chen, W., He, C., Xu, L., Li, H., Zhang, Y., & Fang, Z. (2024). Natural biochar catalyst: Realizing the co-valorization of waste cooking oil into high-quality biofuel and carbon nanotube precursor via catalytic pyrolysis process. *Chemical Engineering Journal*, *486*, 150195. https://doi.org/10.1016/J.CEJ.2024.150195

Supplementary Files

This is a list of supplementary files associated with this preprint. Click to download.

- Materialsupl21Set2026.docx